

# Nitrogen-Doped Graphene Quantum Dots Incorporated into MOF-Derived NiCo Layered Double Hydroxides for Nonenzymatic Lactate Detection in Noninvasive Biosensors

Ling-Yu Chang, Mia Rinawati, Yi-Ting Guo, Yu-Chi Lin, Chia-Yu Chang, Wei-Nien Su, Hitoshi Mizuguchi, Wei-Hsiang Huang, Jeng-Lung Chen, and Min-Hsin Yeh\*



Cite This: *ACS Appl. Nano Mater.* 2024, 7, 14431–14442



Read Online

ACCESS |



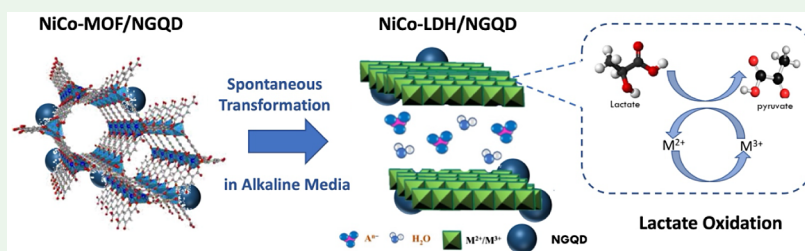
Metrics & More



Article Recommendations



Supporting Information



**ABSTRACT:** Rapid interest in identifying specific biomarkers has been sparked by the development of wearable electrochemical sensors for physiological and biological monitoring via noninvasive measurement. During anaerobic metabolic circumstances, monitoring the lactate content become critical for noninvasive diagnostic of hypoxia. To improve the sensitivity of wearable sweat biosensors for detecting lactate concentrations, in this study, metal–organic framework (MOF)-derived NiCo-based layered double hydroxides (*m*-NiCo LDHs) with N-doped graphene quantum dots (NGQDs) decoration are designed. According to the X-ray absorption spectroscopy (XAS) analysis, the incorporation of NGQDs will alter the local electronic structure of transition metals in *m*-NiCo LDHs, thereby reducing the charge transfer resistance and accelerating the electron transfer kinetics during electrochemical reactions of lactate detection. After understanding the role of NGQDs in the matrix of *m*-NiCo LDHs, as-designed NGQD/*m*-NiCo LDH-based electrochemical biosensors for lactate detection displayed superior sensitivity of  $62.63 \pm 1.50 \mu\text{A mM}^{-1} \text{cm}^{-2}$  under an applied potential of 0.60 V (vs Ag/AgCl/3 M KCl) with the lactate concentration range of 0 to 15 mM in alkaline condition, compared to pristine NiCo LDH ( $16.77 \pm 1.70 \mu\text{A mM}^{-1} \text{cm}^{-2}$ ) and *m*-NiCo LDH ( $45.45 \pm 4.39 \mu\text{A mM}^{-1} \text{cm}^{-2}$ )-based ones. This research provides a potential electrocatalyst of GQD-modified MOF-derived LDHs for using enzyme-free electrochemical lactate sensors with reliable and stable performance in order to implement noninvasive human perspiration monitoring on wearable bioelectronics.

**KEYWORDS:** graphene quantum dots, lactate, layered double hydroxides, metal–organic framework, enzyme-free, noninvasive

## INTRODUCTION

The advent of noninvasive sensors in healthcare and biomedical monitoring systems has revolutionized the continuous measurement of vital biomarkers (e.g., fluid, saliva, blood, and sweat), leading to notable advancements in disease tracking, health assessment, and medical diagnostics. These sensors have shown to be excellent alternatives to invasive biosensors, providing noninvasive, online, and real-time health monitoring capabilities.<sup>1,2</sup> Sweat, on the other hand, presents a promising avenue for molecular-level real-time monitoring of an individual's health status, thanks to its accessibility and diverse composition. With its ease of access and rich molecular content, sweat holds tremendous potential for tracking and assessing an individual's well-being in real time.<sup>3,4</sup> A typical biosensor comprises two essential components: a receptor (such as an antibody, DNA, or enzyme) and a transducer. The

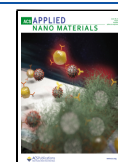
receptor identifies and interacts with the target biomolecule, while the transducer uses mechanical, optical, or electrochemical mechanisms to turn this biorecognition event into a readily detectable signal.<sup>5,6</sup> Recent breakthroughs have led to the development of biosensors capable of detecting sweat biomolecules, such as uric acid, glucose, and lactate, noninvasively for either *in vivo* or *in vitro*. These biomolecules have critical roles in physiological and therapeutic contexts.<sup>7,8</sup>

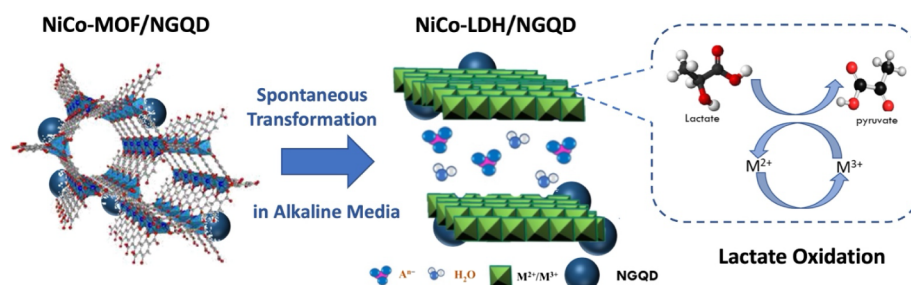
**Received:** April 2, 2024

**Revised:** May 20, 2024

**Accepted:** May 27, 2024

**Published:** June 6, 2024



Scheme 1. Schematic Illustration of Lactate Detection via NGQD/*m*-NiCo LDH

To assess the intensity of exercise under anaerobic metabolic conditions and prevent metabolic acidosis and fatigue from excessive exercise, lactate works as an essential biomarker among the numerous metabolites within the human body.<sup>9,10</sup> In recent years, numerous analytical techniques for lactate detection have been developed, such as fluorometry, colorimetry, nuclear magnetic resonance, gas chromatography, and high-performance liquid chromatography.<sup>11–15</sup> However, the major challenges are complex lengthy pretreatment processes, high costs, and low efficiency.<sup>16</sup> When compared to other techniques, the electrochemistry technique is the preferred method for sweat monitoring due to its ability to provide real-time analysis, potential for miniaturization, relatively high sensitivity, and rapid responsiveness.<sup>17</sup> Lactate detection in an analyte requires bioreceptor enzymes, such as lactate oxidase and lactic dehydrogenase. Based on the detection procedure, the electrochemical lactate biosensor with enzyme immobilization possessed exceptional selectivity and high sensitivity. Nevertheless, the applicability of enzyme-based biosensors in electronics may be limited by insufficient long-term consistency and environmentally sensitive characteristics inherent to enzymes. To address this issue, the development of electrocatalysts to recognize targets for nonenzymatic biosensor has also been investigated in the past few years.<sup>18–23</sup>

Transition metal layered double hydroxides (LDHs), a class of anionic clays, have garnered significant attention as promising materials with distinctive chemical and physical properties for electrocatalytic applications, owing to their ability to adjust metal ions within the layers, facile interchangeability of intercalated anions, large specific surface area, and high redox activity.<sup>24,25</sup> Based on these advantages, LDHs have several benefits that make them highly promising materials in various domains, including electrocatalysis, electrochemical sensing, analytic chemicals, biomedicine, and others.<sup>26–28</sup> These advantages contribute to their exceptional performance in these applications. Ni and Co in LDHs are regarded as promising candidates for electrocatalytic fields due to the fact that Ni and Co have a synergistic effect on electrocatalysis reactions by virtue of their layered structure.<sup>29</sup> Furthermore, the utilization of metal–organic framework (MOF) precursor templates,<sup>30,31</sup> has emerged as a fruitful avenue for enhancing electron transport and binding site coordination with unsaturated sites in subsequent modifications, owing to their complex topologies, high porosity, and large surface area. Recent research has focused on the synthesis of complex-structured topologies that possess high surface area and porous precursor templates, such as MOFs that have demonstrated its usefulness in supplying extra active sites required for catalytic activity, thereby improving the total catalytic performance.<sup>32</sup> This innovative approach has

significantly contributed to the design and derivation of metal-based materials. In general, pristine MOFs are incapable of application in energy storage and conversion owing to its inert nature and instability. Thus, transforming them to LDHs will be beneficial to overcome those limitations while regaining the high surface area of the MOF.

To satisfy the ever-increasing demand for the sensing of species of clinical and environmental interest, there is an urgent need to develop novel and highly efficient electrode materials.<sup>33</sup> Moreover, typical LDHs face challenges in the low electrical conductivity that hinders their catalytic activity. Consequently, the development of suitable materials becomes imminent to enhance lactate sensing capabilities. Among the various options, carbon-based substances are the most frequently employed promising materials used in electrochemical applications thanks to their exceptional structures, scalability, and unique characteristics. Diverse allotropes of carbon nanomaterials have been extensively utilized as materials of electrode for numerous sensing applications.<sup>34–36</sup> Their versatility and robustness make them ideal candidates for enhancing the performance of electrochemical sensors.

Graphene quantum dots (GQDs), which are zero-dimensional graphene fragments, have attracted a lot of interest because of their unique optical characteristics and remarkable electrical performance.<sup>37</sup> These properties distinguish GQDs as versatile materials with applications in a variety of fields, including sensors,<sup>37</sup> bioimaging,<sup>38</sup> and others. Notably, GQDs have exceptional conductivity and biocompatibility, distinguishing them from the carbon subclass and making them ideal for biosensing applications. Furthermore, the introduction of a foreign atom into graphene quantum dots (GQDs) can induce structural alterations closely linked to the presence of defects. As an example, a study by Huang et al. demonstrated the development of an electrochemical sensor based on a combination of GQDs and multiwalled carbon nanotubes to detect dopamine release.<sup>39</sup> The  $\pi$ – $\pi$  stacking force caused by conjugated  $\pi$  bonds in GQDs enhanced dopamine electron transport. Furthermore, introducing foreign heteroatoms (such as B and N) with electronegativities different from those of carbon would disrupt the electroneutrality of GQDs, which would result in the formation of regions with redistributed charges and then create additional hot spots for catalytic reaction. Recently, Lin et al. observed a remarkable electrocatalytic performance resulting from the synthesis of nanocomposites consisting of N-doped graphene quantum dots (NGQDs) and modified polyaniline (PANI).<sup>40</sup> This enhanced activity can be due to the electronic modulation that occurs between NGQDs and the conducting polymer. These results highlight GQDs' potential as a versatile yet efficient material in the field of enhanced biosensing technologies.

In this groundbreaking study, we demonstrated the design and development of a novel noninvasive lactate biosensor for human perspiration by incorporating a nanocomposite layer of NGQD/*m*-NiCo LDH, visually depicted in Scheme 1. The well-maintained skeleton structures of MOF supply extra active sites upon their transformation to LDHs, enabling more efficient substrate diffusion and robust electrocatalysts design. Moreover, the intrinsic LDH properties, with their unique layered structures, serve as the favorable host for catalytic reaction, despite their inherent conductivity challenge. Meanwhile, numerous nitrogen functional groups within NGQDs act as highly efficient electron transfer reagents, the key activity in the redox reaction. Thus, the idea to integrate NGQDs in MOF-derived LDHs will be a promising strategy to the lactate detection electroactivity, addressing the shortcomings of the conductivity of the LDH. As a result, our designed NGQD/*m*-NiCo LDH exhibited a lactate detection sensitivity of  $62.63 \pm 1.50 \text{ A mM}^{-1} \text{ cm}^{-2}$  and demonstrated outstanding long-term durability, maintaining its high performance over a 30-day period. These remarkable achievements mark a significant advancement in noninvasive lactate biosensing technology, offering tremendous potential for applications in athletic performance monitoring, healthcare diagnostics, and overall well-being assessment.

## EXPERIMENTAL SECTION

**Materials.** Nickel(II) nitrate hexahydrate ( $\text{Ni}(\text{NO}_3)_2 \cdot 6\text{H}_2\text{O}$ ,  $\geq 98\%$ ) and cobalt nitrate hexahydrate ( $\text{Co}(\text{NO}_3)_3 \cdot 6\text{H}_2\text{O}$ , 99.1%) were supplied from J. T. Baker. Fisher Chemical supplied methanol (99.9%), ethanol (99.8%), N,N-dimethylformamide (DMF,  $\geq 99.5\%$ ), and potassium hydroxide (KOH, ca. 85%). The Tokyo Chemical Industry Co. provided 2,5-dihydroxyterephthalic acid ( $\text{H}_4\text{DOT}$ , 98%). Acros Organics supplied uric acid ( $\geq 99.0\%$ ) and citric acid (99.5%). L-lactate (98.0%), Nafion 117 solution ( $\sim 5\%$ ), and glucose ( $\text{C}_6\text{H}_{12}\text{O}_6$ ,  $\geq 99.5\%$ ) were obtained from Sigma-Aldrich.

**The Synthesis of Graphene Quantum Dots (GQDs) and Nitrogen-Doped Graphene Quantum Dots (NGQDs).** For the synthesis of GQDs,<sup>41</sup> a citric acid solution ( $1 \text{ mg mL}^{-1}$ , 40 mL) was prepared and subjected to sonication. The resulting solution was then heated at  $200^\circ\text{C}$  for 3 h and transferred to a Teflon-lined autoclave. After the synthesis process, a pale-yellow GQD solution was obtained, which was subsequently purified by dialysis against deionized (DI) water for 20 min. The dialysis procedure involved using a dialysis tube and centrifugation at 4000 rpm (Spectrum Lab. Inc., 3000 Da) to remove impurities and unwanted substances. For the synthesis of NGQDs,<sup>40</sup> 5 mL of ammonium hydroxide was added to an aqueous citric acid solution ( $1 \text{ mg mL}^{-1}$ , 40 mL). The mixture was thoroughly mixed until ammonium hydroxide was uniformly dispersed in the solution at room temperature. The resulting solution was then transferred to a Teflon-lined stainless-steel autoclave for a 3-h hydrothermal treatment at  $200^\circ\text{C}$ . To eliminate any unreacted compounds and contaminants, the obtained solution underwent dialysis using a 3000 Da dialysis tube (Spectrum Lab, Inc.). This purification step ensured the removal of residual components, resulting in a purified NGQD solution that was ready for further characterization and applications.

**Synthesis of NiCo MOF and NGQD/NiCo MOF.** NiCo MOF was produced via the coprecipitation method. Briefly,  $\text{H}_4\text{DOT}$  (0.45 mmol), nickel nitrate (0.36 mmol), and cobalt nitrate (0.36 mmol) were dissolved and ultrasonicated in a

mixed solution consisting of DMF (30.0 mL), ethanol (1.8 mL), and  $\text{H}_2\text{O}$  (1.8 mL) for half an hour. The solution was then transferred to a 100 mL Teflon-lined stainless steel autoclave for 24 h with heat treatment at  $120^\circ\text{C}$ . The products were collected through centrifugation, washed many times with methanol and ethanol, and then dried overnight at  $60^\circ\text{C}$  under vacuum. The NGQD/NiCo MOF was produced by the same process, except for an extra NGQD solution (0.5 mL) that was added at the first step.

**Synthesis of MOF-Derived LDHs.** To obtain MOF-derived LDHs, NiCo MOF and NGQD/NiCo MOF were immersed in a 1 M KOH solution and subjected to ultrasonication to ensure thorough homogenization. The resulting solution was then moved into the Teflon-lined autoclave and subjected to heating at  $120^\circ\text{C}$  for 2 h, allowing for the transformation of the MOF into LDHs. Following this step, the obtained LDH products underwent multiple washes using deionized (DI) water and ethanol to remove any residual impurities. Subsequently, the samples were dried at  $60^\circ\text{C}$  to yield the final products. The resulting powder were denoted as *m*-NiCo LDH and NGQD/*m*-NiCo LDH.

**Preparation of MOF-Derived LDH-Modified Electrodes.** SPCE was used as a substrate for analyzing the electrochemical performance and sensing properties. Each sample of LDHs was subsequently added to a mixture solvent IPA: DI water: Nafion (14:5:1). On the SPCE surface, 60  $\mu\text{L}$  of LDH solution (3 mg/mL) was drop-coated to produce MOF-derived LDH/SPCE electrodes. Finally, after the electrode was kept at ambient temperature to permit evaporation of the solvent, MOF-derived LDHs were coated on SPCE.

**Material Characterization.** The surface morphology and composition of as-prepared materials was explored by scanning electron microscopy (SEM, JSM-6500F, JEOL Japan), energy-dispersive X-ray spectroscopy (EDS, detector model 7418, Oxford, UK), and field-emission transmission electron microscopy (TEM, JEM-2100F, JEOL, Japan). Crystallinity of as-prepared materials was performed by an X-ray diffractometer (XRD, D2 Phaser, Bruker, USA) with Cu K $\alpha$  radiation ( $\lambda=1.5418 \text{ \AA}$ ). X-ray photoelectron spectroscopy (XPS, PHI 5000 VersaProbe III, ULVAC-PHI, Inc., Japan) was utilized to investigate the chemical states of the as-prepared materials. Raman spectra were acquired using a micro-Raman system (UniNanoTech, UniRAM, Korea) with a 532 nm green laser and a CCD detector. Ni and Co K-edge X-ray absorption spectroscopy (XAS) was utilized to analyze the electronic and local structure of the materials with the 17C1 beamline at the National Synchrotron Radiation Research Center (NSRRC) in Taiwan. Athena software was used to normalize all of the spectra. The excitation and emission spectra of photoluminescence (PL) spectroscopy for NGQD solution were recorded using a commercial spectrometer (Nanolog-3 spectrofluorometer, Horiba Jobin Yvon, France) with a 20 nm bandpass for both emission and excitation and an InGaAs NIR detector.

**Electrochemical Measurement.** The cyclic voltammetry (CV) and electrochemical impedance spectroscopy (EIS) were conducted in a standard three-electrode electrochemical cell with the modified SPCE as the working electrode (WE), a platinum sheet as the counter electrode (CE), and Ag/AgCl (3 M KCl) as the reference electrode (RE). We investigated the chronoamperometric response of modified electrodes by injecting 0–22.5 mM lactate into MOF-derived LDH-modified



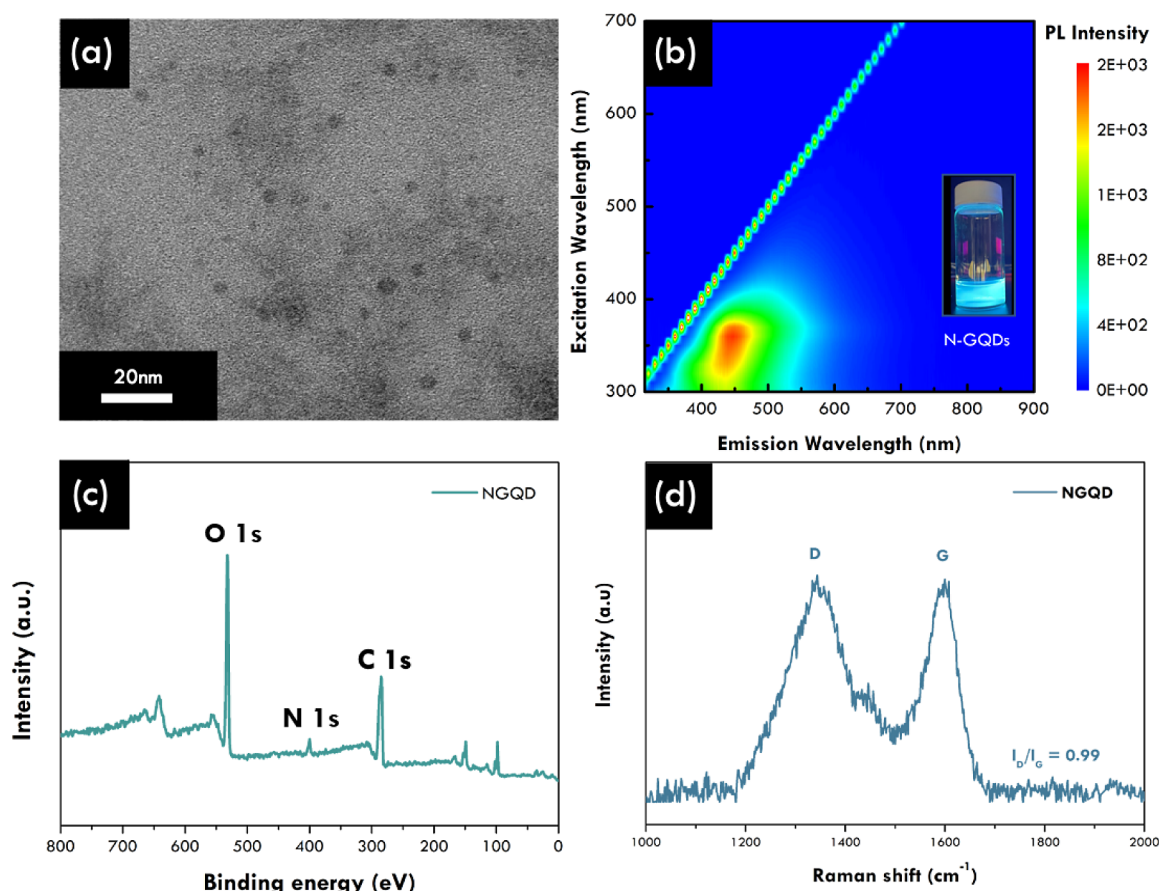


**Figure 1.** (a) TEM images of NGQDs, (b) PL excitation–emission intensity spectra of NGQDs. Inset: NGQDs under 365 nm UV (c) XPS survey scan of NGQDs, (d) the Raman spectra of NGQD.

electrodes during amperometric measurement in 0.1 M NaOH. In addition, the double-layer capacitance of as-prepared modified electrodes was determined by cyclic voltammetry at various scan rates (20, 40, 60, 80, and 100  $\text{mV s}^{-1}$ ) in order to calculate the electrochemically active surface area (ECSA) in 0.1 M NaOH.

## RESULTS AND DISCUSSION

**Characterization of NGQD.** To investigate the morphology of the as-synthesized NGQDs, transmission electron spectroscopy (TEM) was used, as shown in Figure 1a. The TEM image clearly illustrated the as-synthesized NGQDs had regular particle size distribution (3–5 nm) with an average size distribution of  $3.5 \pm 0.38$  nm (Figure S1), which indicates that NGQDs with uniform particle size were synthesized successfully. The HR-TEM image (Figure S2) presented a distinct lattice fringe, showcasing a well-defined interplanar spacing of 0.214 nm. This observation signifies the robust crystallinity of the material, aligning precisely with the hexagonal lattice spacing observed along the (100) direction inherent in the graphene structure.<sup>42</sup> Furthermore, the unique photoluminescence (PL) feature of NGQDs was identified, which exhibited strong fluorescence due to their quantum intensity and edge effects.<sup>43</sup> As shown in Figure 1b, the PL excitation–emission-intensity spectra of NGQDs exhibited an excitation wavelength at 360 nm giving a strong emission centered at 440 nm. Blue fluorescence was observed under 365 nm UV light, corresponding to the presence of NGQDs. Moreover, the NGQD aqueous solution emanated blue light

on exposure to 365 nm UV light, as shown in the inset of Figure 1b. The blue PL emission from NGQD-isolated  $\text{sp}^2$ -hybridized clusters has been attributed to both size and surface effects, which caused the localization of electron–hole pairs generates band gaps with blue emission.<sup>44</sup> To confirm that heteroatomic N was doped into the matrix of GQDs, XPS was employed for characterizing the surface composition. Figure 1c presents the wide scan of XPS for NGQDs with N 1s (401 eV) peak and the C 1s (285 eV) and O 1s (533 eV) peaks. The XPS survey scans for both pristine GQDs (Figure S3) and NGQDs exhibit congruent peaks corresponding to C and oxygen O elements. Notably, the NGQD spectrum reveals additional peaks attributable to nitrogen (N), confirming successful nitrogen doping within the graphene quantum dots. Furthermore, Raman spectroscopy was used to understand the crystallinity disorder of GQDs with heteroatomic N doping, as revealed in Figure 1d. NGQDs show two notable peaks at  $\sim 1340$  and  $\sim 1600$   $\text{cm}^{-1}$ , which are attributed to the existence of well-defined D and G bands, respectively.<sup>45</sup> The degree of disorder, which was defined by the ratio of peak intensity ( $I_D/I_G$ ), the value of NGQDs reaching 0.99, confirmed that considerable defects were generated in the structure of GQDs lattice by N doping.<sup>40</sup>

**Characterization of NGQD/NiCo MOF and NGQD/*m*-NiCo LDH.** The morphology of the NGQD-decorated NiCo MOF (NGQD/NiCo MOF) and NGQD-decorated NiCo MOF-derived layered double hydroxide (NGQD/*m*-NiCo LDH) was investigated by scanning electron microscopy (SEM), as presented in Figure 2a,b, respectively. The typical

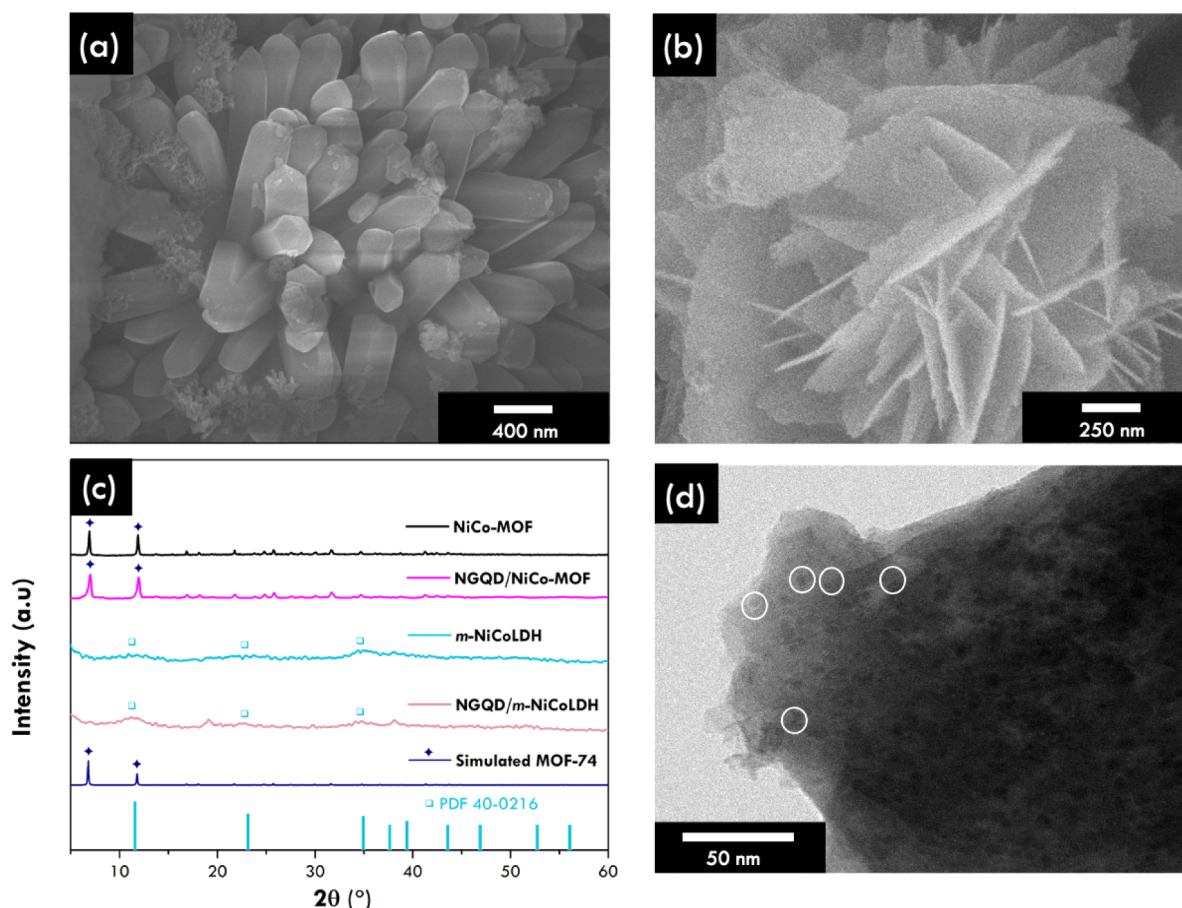


**Figure 2.** SEM images of (a) NGQD/NiCo MOF and (b) NGQD/*m*-NiCo LDH; (c) XRD pattern of NiCo MOF, NGQD/NiCo MOF, *m*-NiCo LDH, and NGQD/*m*-NiCo LDH; and (d) TEM image of NGQD/*m*-NiCo LDH.

cubic-like structure was observed from NGQD/NiCo MOF, which was similar to the morphology of the pristine NiCo MOF (Figure S2a). After that, as-prepared NiFe MOF and NGQD/NiCo MOF were transformed into MOF-derived NiCo layered double hydroxide (*m*-NiCo LDH) and NGQD-modified MOF-derived NiCo layered double hydroxide (NGQD/*m*-NiCo LDH) after immersing in an alkaline solution at room temperature, which was followed by our reported process.<sup>26</sup> The corresponding morphology of *m*-NiCo LDH and NGQD/*m*-NiCo LDH is presented in Figures 2b and S4b, respectively, which explored that the nanosheet-like structure was formed after transformation and suggested that the transformation mechanism was consisted after adding NGQDs into the matrix of NiCo MOF. To confirm the chemical states of NGQD/*m*-NiCo LDH after transformation, X-ray absorption spectrum (XAS) was conducted to explore the valence state of transition metal. X-ray absorption near edge structure (XANES) spectra of Ni K-edge (Figure S4c) revealed distinct spectra of *m*-NiCo LDH to NiCo MOF, suggesting the transformation from MOF to LDH. In the same way, the Co K-edge showed a similar pattern between *m*-NiCo LDH and NiCo MOF, which further proved the process of change. X-ray diffraction (XRD) analysis was utilized to ascertain the successful transformation of NGQD/*m*-NiCo LDH from the MOF. The crystalline nature of both NGQD/NiCo MOF and NGQD/*m*-NiCo LDH was examined, as depicted in Figure 2c. For the purpose of comparison, NiCo MOF and *m*-NiCo LDH were also included in the study. All

diffraction peaks of NGQD/NiCo-MOF-74 and NiCo-MOF-74 correspond precisely to the simulations presented in the literature, that exhibit a well-matched double peak attributed to the (110) and (300) crystal plane, aligning closely with the simulated pattern, revealing that the structure of MOF was still maintained after introducing NGQDs.<sup>46</sup> On the other hand, for the cases of MOF-derived LDHs, the result of XRD clearly revealed that all the corresponding peaks associated with MOFs have completely transformed into the pattern of LDHs (as referenced by JCPDS No. 40-0216), confirming the successful transformation to LDH,<sup>47</sup> as shown in Figure 2c. To confirm that the embedded NGQDs in the matrix of NiCo MOF still remained after transformation, the microstructure of NGQD/*m*-NiCo LDH was characterized by TEM, as presented in Figure 2d. The TEM image of NGQD/*m*-NiCo LDH clearly revealed that NGQDs were uniformly distributed within the structure with the particle size ~3.5 nm, which was in agreement with the TEM images of pristine NGQDs (Figure 1a).

**XAS Analysis of NGQD/NiCo MOF and NGQD/*m*-NiCo LDH.** To gain a deeper understanding of the interaction between NGQDs and MOF-derived LDHs, the X-ray absorption near-edge structure (XANES) and extended X-ray absorption fine structure (EXAFS) measurements were conducted to comprehend alterations in the local structural motifs of MOF-derived LDHs. Figure 3a depicts that the Ni K-edge XANES spectra of *m*-NiCo LDH and NGQD/*m*-NiCo LDH were quite similar. However, compared to *m*-NiCo LDH,

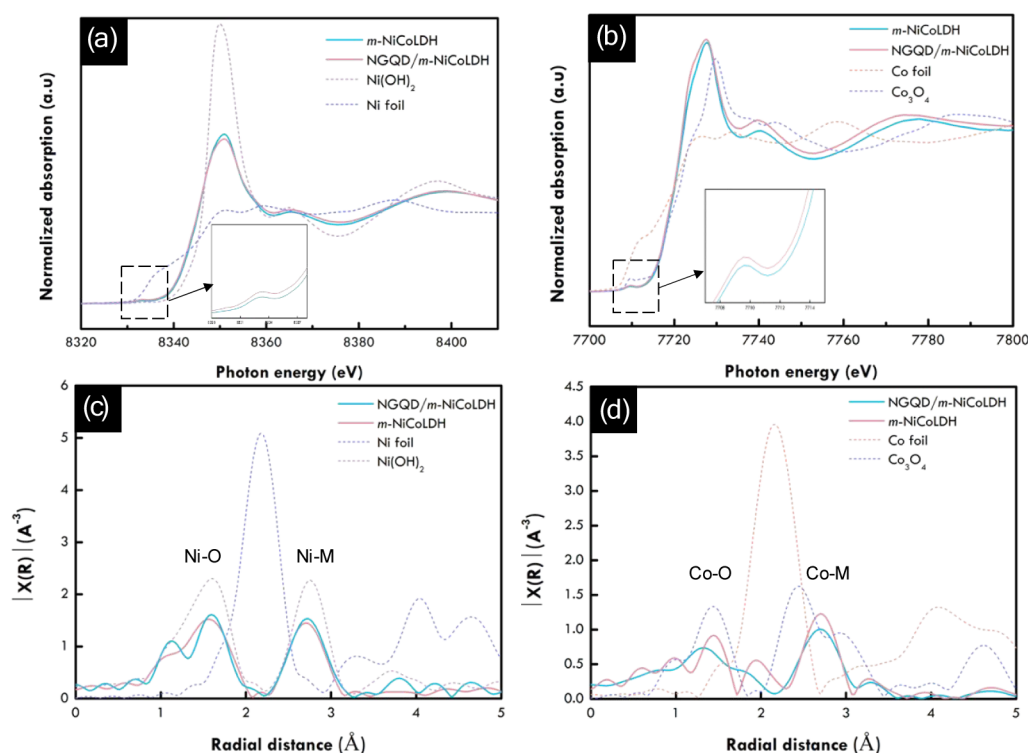


**Figure 3.** XAS measurements of NGQD/*m*-NiCo LDH and *m*-NiCo LDH. Normalized (a) Ni K-edge and (b) Co K-edge XANES spectra. (c) Ni and (d) Co edge Fourier transform magnitudes of  $k^3$ -weighted EXAFS spectra.

the pre-edge peak intensity of NGQD/*m*-NiCo LDH is significantly lower, indicating structural disorder and the presence of defects in NGQD/*m*-NiCo LDH.<sup>48</sup> The pre-edge at about 8330 eV originates from the transition of  $1s \rightarrow 3d$ . The decrease of prepeak intensity implies that Ni receives some charges and the local structure surrounding Ni becomes noncentrosymmetric.<sup>49</sup> Additionally, intense absorption edge peaks of *m*-NiCo LDH were observed, associated with the slightly higher oxidation state of the Ni. The Co K-edge XANES spectra are shown in Figure 3b. Similar observations were also made on the XANES spectra of the Co K-edge. Interestingly, the absorption edge peak of *m*-NiCo LDH was decreased than that of NGQD/*m*-NiCo LDH, suggesting the higher oxidation state of the Co in NGQD/*m*-NiCo LDH. The Fourier transform of the extended X-ray absorption fine structure (FT-EXAFS) are displayed in Figure 3c,d. The abscissas of Ni and Co K-edge Fourier transform in R space, corresponding to the bond lengths of metal–oxygen and metal–metal, respectively. For the Ni FT-EXAFS, it exhibited two major coordination peaks at  $\sim 1.5$  and  $\sim 2.7$  Å, corresponding to the typical M–O bond and M–M bond, respectively. It is then worth noting that M–O are split to two types of metal–oxygen bonds after NGQD was introduced to *m*-NiCo LDH, implying two forms of Ni–O bonds in tetrahedral coordination: One is the coordination of oxygen from the host layer with the apex anion to form a Ni–O bond (bond length  $\sim 1.5$  Å) and the second is the oxygen shared by the tetrahedron and octahedron (bond length  $\sim 1.9$  Å).<sup>50</sup> Upon the introduction of NGQD, the peak intensity was slightly higher, suggesting locally distorted structure of *m*-NiCo LDH. Similarly, the Co FT-EXAFS exhibited two notable peaks at  $\sim 1.5$  and  $\sim 2.7$  Å, corresponding to the Co–O and Co–M bonds. While the typical bonds were similar, a distinctive shift to the shorter radius was observed in the

Co–O bonds of NGQD/*m*-NiCo LDH, indicating the formation of shorter Co–O bonds after the introduction of NGQD. Thus, the NGQD induced local structure distortion of *m*-NiCo LDH. These sites with shorter bonds (first shell) was particularly more favorable for the electrochemical reaction.<sup>51</sup> Following the introduction of NGQD into *m*-NiCo LDH, the rapid electron interaction and local structure change are expected to facilitate charge transport and accelerate the kinetics during electrochemical reactions, thereby enhancing the lactate sensing performance.

**Electrochemical Performance of NGQD/*m*-NiCo LDH with Various NGQD Loadings.** The electrochemical performance of NGQD/*m*-NiCo LDH with various NGQD loadings for electrochemical lactate detection was investigated by chronoamperometric analysis, as shown in Figure 4a. Among the SPCEs with various NGQD loadings of NGQD/*m*-NiCo LDH, 0.5 mL of NGQD/*m*-NiCo LDH-modified SPCE demonstrated the highest current density under identical lactate concentrations. This observation suggests that 0.5 mL of NGQD/*m*-NiCo LDH-modified SPCE exhibits the highest electrochemical performance for lactate monitoring in comparison to the others. The sensitivity for lactate detection by corresponding SPCEs is presented in Figure 4b, where the results indicated that the SPCE with 0.5 mL NGQD/*m*-NiCo LDH had the highest sensitivity of  $62.63 \pm 1.50 \mu\text{A mM}^{-1} \text{cm}^{-2}$  for sensing lactate, compared to SPCEs with 0.25 mL NGQD/*m*-NiCo LDH ( $35.53 \pm 2.95 \mu\text{A mM}^{-1} \text{cm}^{-2}$ ), 1.0 mL NGQD/*m*-NiCo LDH ( $43.02 \pm 2.53 \mu\text{A mM}^{-1} \text{cm}^{-2}$ ), and 1.5 mL of NGQD/*m*-NiCo LDH ( $24.30 \pm 1.79 \mu\text{A mM}^{-1} \text{cm}^{-2}$ ). For the purpose of investigating the exposed active sites, the relative electrochemical surface area (ECSA) of the electrocatalyst was reflected by the double-layer capacitances ( $C_{dl}$ ). CVs of SPCE with various NGQD loadings of NGQD/*m*-NiCo LDH at various scan rates were used to



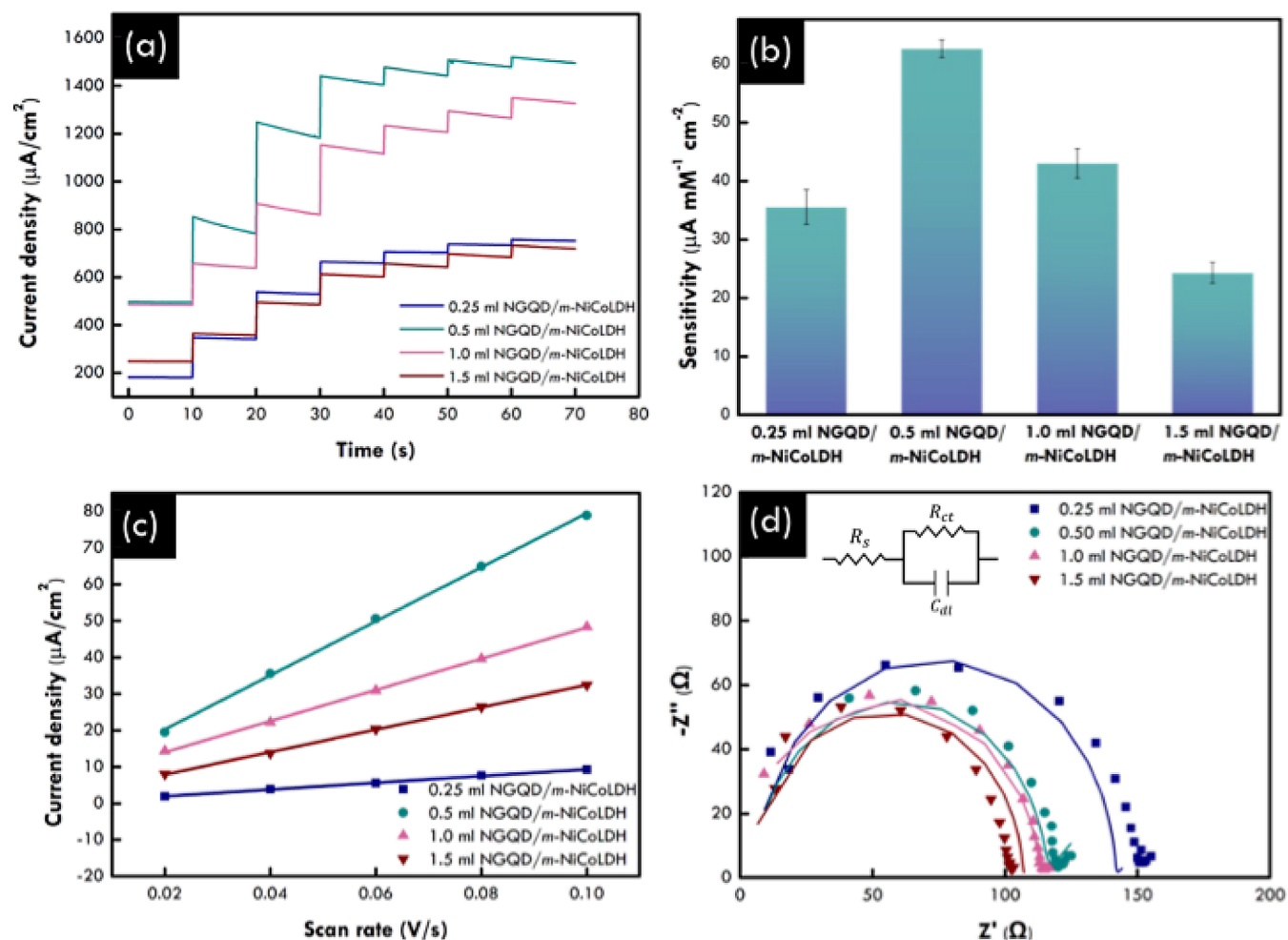


**Figure 4.** (a) Amperometry curve of NGQD/*m*-NiCo LDH-based SPCE with a linear range of 0–22.5 mM lactate, (b) sensitivity corresponding to NGQD/*m*-NiCo LDH, and (c) the double-layer capacitances, and (d) the Nyquist plot of NGQD/*m*-NiCo LDH SPCE; inset showing the electrical equivalent circuit used to simulate the Nyquist plots, where  $R_s$  is the electrolyte resistance,  $R_{ct}$  is the charge-transfer resistance, and  $C_{dl}$  represents the double-layer capacitance.

determine the corresponding  $C_{dl}$  value in 0.1 M NaOH containing 10 mM lactate (Figure S5). This result (Figure 4c) demonstrated conclusively that 0.5 mL of NGQD/*m*-NiCo LDH had the highest  $C_{dl}$  value of  $0.427 \text{ mF cm}^{-2}$ , which is in good agreement with the outstanding sensitivity of lactate detection owing to the synergistic effect between NGQDs and MOF-derived NiCo LDHs.<sup>52</sup> In contrast, an excessive amount of NGQD in the matrix of MOF-derived LDHs may hinder electrochemical performance due to the severe aggregation during the synthesis process,<sup>53</sup> and it was found that as the NGQD content of the composite increased, so did the tendency of the material to aggregate, as shown in Figure S6. EIS measurement further revealed the Nyquist plot of SPCE with various NGQD loadings of NGQD/*m*-NiCo LDH, as shown in Figure 4d. For EIS measurement, the frequency range explored was from 100 kHz to 10 mHz with the corresponding ac amplitude of 10 mV under applied potential of 0.60 V (vs 3 M Ag/AgCl). Figure 4d presents the Nyquist plots of the catalysts, in which the observed semicircle is mainly attributed to the charge-transfer resistance ( $R_{ct}$ ) at the electrode–electrolyte interface. The result clearly demonstrated that the value of  $R_{ct}$  decreases as the NGQD quantity increases in NGQD/*m*-NiCo LDH, which revealed that the charge transfer

of the *m*-NiCo LDH/electrolyte could be facilitated by NGQD integration.

**Electrochemical Performance of *p*-NiCo LDH, *M*-NiCo LDH, and NGQD/*m*-NiCo LDH.** To reveal the enhancement of *m*-NiCo LDH with NGQD modification for lactate detection, the catalytic activity of NGQD/*m*-NiCo LDH and *m*-NiCo LDH for lactate detection in 0.1 M NaOH was determined by cyclic voltammetry (CV), as depicted in Figure S7. It can be found that the current density of NGQD/*m*-NiCo LDH was obviously higher than that of *m*-NiCo LDH, implying that the electrocatalytic activities of *m*-NiCo LDH for lactate oxidation could be boosted by introducing NGQD. A comparative examination of CV curve regions shows an increasing order in the current density, NGQD/*m*-NiCo LDH > *m*-NiCo LDH, suggesting an increase in electrical conductivity, highlighting the beneficial effect of NGQD integration. To make a comparison, pristine NiCo LDH (*p*-NiCo LDH) was included in this study as well.<sup>28</sup> The amperometric response of *p*-NiCo LDH, *m*-NiCo LDH, and NGQD/*m*-NiCo LDH-based SPCE with different concentrations of the lactate (0–22.5 mM) under the applied potential of 0.60 V (vs 3 M Ag/AgCl) is shown in Figure 5a. Figure 5b depicts the calibration curves of the corresponding SPCEs for lactate detection, which revealed that the NGQD/

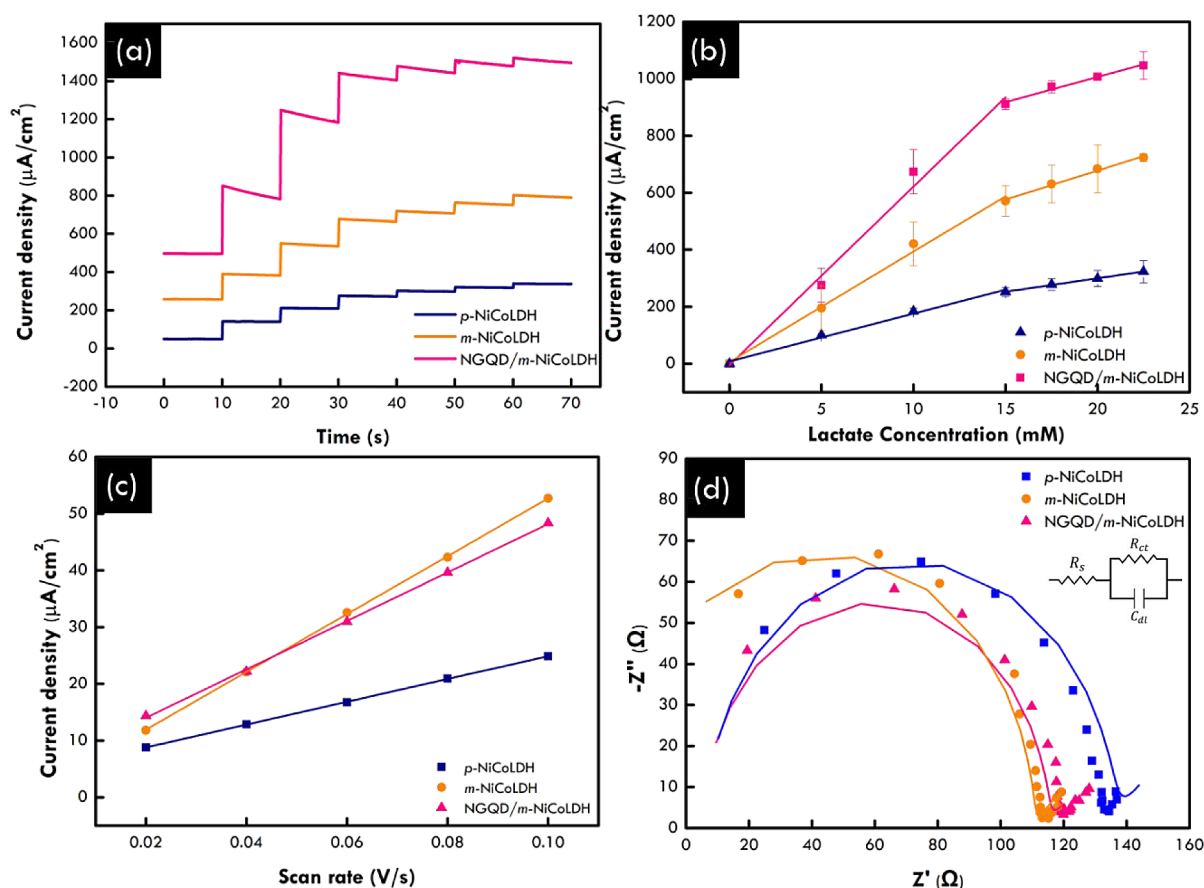


**Figure 5.** (a) Amperometry response, and (b) the matching calibration curve of SPCE with *p*-NiCo LDH, *m*-NiCo LDH, and NGQD/*m*-NiCo LDH for a linear range of 0–22.5 mM lactate; (c) the double layer capacitance, and (d) the Nyquist plot of *p*-NiCo LDH, *m*-NiCo LDH, and NGQD/*m*-NiCo LDH SPCE in the presence of 10 mM lactate in 0.1 M NaOH at 0.60 V (V vs Ag/AgCl/3 M KCl); inset showing the electrical equivalent circuit used to simulate the Nyquist plots, where  $R_s$  is the electrolyte resistance,  $R_{ct}$  is the charge-transfer resistance, and  $C_{dl}$  represents the double-layer capacitance.

*m*-NiCo LDH-based SPCE demonstrated a linear response from 0 to 15 mM lactate. Moreover, the sensitivity of the SPCE with NGQD/*m*-NiCo LDH was  $62.63 \pm 1.50 \mu\text{A mM}^{-1} \text{cm}^{-2}$  ( $R^2 = 0.994$ ), which was greater than that of the SPCEs with *m*-NiCo LDH ( $45.45 \pm 4.39 \mu\text{A mM}^{-1} \text{cm}^{-2}$ ,  $R^2 = 0.9972$ ) and *p*-NiCo LDH ( $16.77 \pm 1.70 \mu\text{A mM}^{-1} \text{cm}^{-2}$ ,  $R^2 = 0.9962$ ), implying that *m*-NiCo LDH decorated with NGQD can achieve a higher catalytic activity for lactate detection. In addition, the values of  $C_{dl}$  for *p*-NiCo LDH, *m*-NiCo LDH, and NGQD/*m*-NiCo LDH-based SPCE were evaluated and presented in Figure 5c (corresponding CV curves are presented in Figure S8). Surprisingly, NGQD/*m*-NiCo LDH exhibited a nearly identical  $C_{dl}$  value of  $0.427 \text{ mF cm}^{-2}$  in comparison with *m*-NiCo LDH ( $0.509 \text{ mF cm}^{-2}$ ), followed by *p*-NiCo LDH ( $0.207 \text{ mF cm}^{-2}$ ), which indicated that the enhanced catalytic activity of MOF-derived LDH is attributed to the newly exposed crystal planes that provide additional active sites for catalytic pathways.<sup>54</sup> Moreover, as presented in Figure 5d, EIS results indicated that the *m*-NiCo LDH-based SPCE has the larger  $R_{ct}$  value of  $136.7 \Omega$ . Notably, the value of  $R_{ct}$  of SPCE with NGQD/*m*-NiCo LDH decreased ( $109 \Omega$ ), confirming that the NGQD enhanced the interfacial electron transport.<sup>55</sup> In addition, the electrochemical performance of NGQD/*m*-NiCo LDH for lactate detection surpasses the vast majority of previously reported electrocatalysts, as shown in Table S1.

**Limit of Detection, Interference Test, Reproducibility, and Long-Term Stability Test of NGQD/*m*-NiCo LDH-Based Nonenzymatic Lactate Biosensor.** The limit of detection (LOD) of an analyte is the lowest concentration that the biosensor can detect during a test for analysis. The LOD is determined by  $\text{LOD} = 3S_b/m$ , where  $m$  represents the slope of the calibration curves and  $S_b$  is the deviation standard of amperometric test for the null signal. Figure S8 shows that the LOD of the NGQD/*m*-NiCo LDH-based SPCE for lactate is  $0.252 \text{ mM}$ , which is substantially lower than the lactate content in human sweat ( $1\text{--}20 \text{ mM}$ ). This result suggests that the NGQD/*m*-NiCo LDH-based SPCE could be utilized in a nonenzymatic lactate biosensor to detect lactate concentrations in human perspiration noninvasively. To further evaluate the selectivity of the NGQD/*m*-NiCo LDH-based SPCE, an interference test was performed with a number of prevalent chemical compounds that also exist in human perspiration (such as glucose, ascorbic acid, and uric acid). Figure 6a depicts that the results of interference tests revealed a distinct response from the NGQD/*m*-NiCo LDH-based SPCE after the injection of 5 mM lactate, whereas only minor fluctuations were observed after the addition of  $20 \mu\text{M}$  uric acid,  $25 \mu\text{M}$  ascorbic acid, and  $25 \mu\text{M}$  glucose. This result conclusively demonstrates that the NGQD/*m*-NiCo LDH-based SPCE has remarkable selectivity for lactate detection despite the presence of interference deviation in human



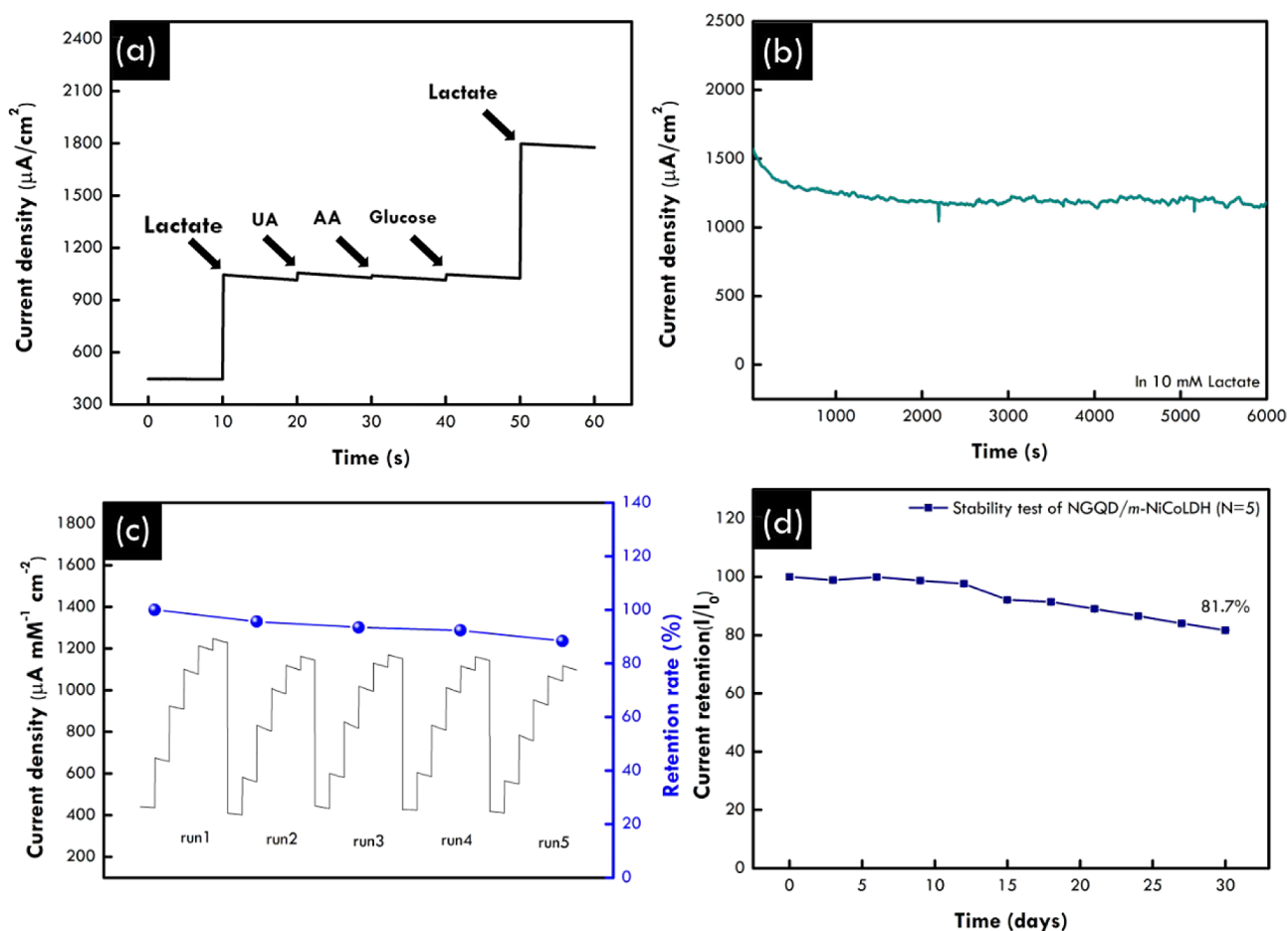


**Figure 6.** (a) Interference test by amperometric response in the presence of various substances in 0.1 M NaOH. (b) The stability test, (c) the repeatability test on 5 individual running, and (d) long-term stability test with 10 mM lactate in 0.1 M NaOH.

perspiration. The repeatability and stability of the NGQD/*m*-NiCo LDH-based SPCE were evaluated to expand the potential implements for noninvasive biosensors, as shown in Figure 6b, which demonstrates insignificant current decrease while lactate concentrations are constantly monitored at 10 mM. With a retention of 92.9% after 6000 s of measurement, the corresponding current signal was stable and attested for constant monitoring. Furthermore, five separate repeatability tests of the NGQD/*m*-NiCo LDH-based SPCE were conducted, as shown in Figure 6c, where the sensitivity retention rate was 88.4% after individual tests 5 times.

In addition, after 30 days of storage at room temperature, the NGQD/*m*-NiCo LDH-based SPCE still retained 81.7% of its initial sensitivity (Figure 6d). This provided limitless opportunities to incorporate NGQD/*m*-NiCo LDH into numerous electrochemical lactate biosensors with superior sensitivity and endurance. The nonenzymatic electrochemical sensor with NGQD/*m*-NiCo LDH proposed in this work was also a potential substrate for incorporation into a wearable electronic device for determining the concentration of lactate in the body's biofluids in order to monitor the health condition.

## CONCLUSION

In this study, we effectively engineered NGQD/*m*-NiCo LDH, a nanocomposite material formed through the spontaneous derivation of NGQD/NiCo MOF under alkaline conditions.

This material served as an electrode in the development of an electrochemical biosensor for lactate monitoring. Our TEM results confirmed the successful integration of NGQDs into the *m*-NiCo LDH matrix, resulting in enhanced electrocatalytic activity for lactate detection. The incorporation of NGQDs into *m*-NiCo LDH led to reduced charge transfer resistance, facilitating rapid electron transfer kinetics during lactate detection. Furthermore, the fine-tuning of the transition metal local structure by NGQDs drastically increased the lactate detection sensitivity of NGQD/*m*-NiCo LDH, reaching a remarkable sensitivity of  $62.63 \pm 1.50 \mu\text{A mM}^{-1} \text{cm}^{-2}$ . Notably, the NGQD/*m*-NiCo LDH-modified screen-printed carbon electrode demonstrated high selectivity, reproducibility, and long-term stability. It maintained an outstanding stability of 88.36% throughout a rigorous 30-day testing period, making it exceptionally reliable for long-term usage. This stability enables the utilization of NGQD/*m*-NiCo LDH in a wide range of lactate electrochemical sensors with both high sensitivity and long-lasting performance. The electrochemical biosensor based on NGQD/*m*-NiCo LDH shows major potential as an enzyme-free lactate biosensor, allowing noninvasive monitoring of body biofluids to gain vital insights into human metabolic levels and muscle fatigue. This integrated cutting-edge biosensing technology offers new possibilities for real-time, noninvasive lactate testing, with implications for enhanced sports performance monitoring, healthcare diagnostics, and general well-being assessment.

## ■ ASSOCIATED CONTENT

### SI Supporting Information

The Supporting Information is available free of charge at <https://pubs.acs.org/doi/10.1021/acsanm.4c01899>.

Pretreatment process of screen-printed carbon electrode (SPCE), the particle size distribution of NGQD, HR-TEM image and XPS of NGQD, SEM images and hard-XAS of NGQD/NiCo-MOF74 and NGQD/*m*-NiCo LDH, SEM images and CV curves of NGQD/*m*-NiCo LDH with various concentrations of GQDs, LOD measurements, and comparison table for nonenzymatic lactate detection in NaOH (PDF)

## ■ AUTHOR INFORMATION

### Corresponding Author

**Min-Hsin Yeh** – Department of Chemical Engineering, National Taiwan University of Science and Technology, Taipei 10607, Taiwan; Sustainable Electrochemical Energy Development Center, National Taiwan University of Science and Technology, Taipei 10607, Taiwan; [orcid.org/0000-0002-6150-4750](https://orcid.org/0000-0002-6150-4750); Phone: +886-2-2737-6643; Email: [mhyeh@mail.ntust.edu.tw](mailto:mhyeh@mail.ntust.edu.tw); Fax: +886-2-2737-6644

### Authors

**Ling-Yu Chang** – Department of Chemical Engineering, National Taiwan University of Science and Technology, Taipei 10607, Taiwan

**Mia Rinawati** – Department of Chemical Engineering, National Taiwan University of Science and Technology, Taipei 10607, Taiwan

**Yi-Ting Guo** – Department of Chemical Engineering, National Taiwan University of Science and Technology, Taipei 10607, Taiwan

**Yu-Chi Lin** – Department of Chemical Engineering, National Taiwan University of Science and Technology, Taipei 10607, Taiwan

**Chia-Yu Chang** – Graduate Institute of Applied Science and Technology, National Taiwan University of Science and Technology, Taipei 10607, Taiwan

**Wei-Nien Su** – Graduate Institute of Applied Science and Technology, National Taiwan University of Science and Technology, Taipei 10607, Taiwan; Sustainable Electrochemical Energy Development Center, National Taiwan University of Science and Technology, Taipei 10607, Taiwan; [orcid.org/0000-0003-1494-2675](https://orcid.org/0000-0003-1494-2675)

**Hitoshi Mizuguchi** – Department of Applied Chemistry, Graduate School of Science and Technology, Tokushima University, Tokushima 770-8506, Japan; [orcid.org/0000-0003-2396-6812](https://orcid.org/0000-0003-2396-6812)

**Wei-Hsiang Huang** – National Synchrotron Radiation Research Center, Hsinchu 30076, Taiwan; [orcid.org/0000-0001-9503-0373](https://orcid.org/0000-0001-9503-0373)

**Jeng-Lung Chen** – National Synchrotron Radiation Research Center, Hsinchu 30076, Taiwan

Complete contact information is available at: <https://pubs.acs.org/doi/10.1021/acsanm.4c01899>

### Author Contributions

The manuscript was written through contributions of all authors. All authors have given approval to the final version of the manuscript.

## Notes

The authors declare no competing financial interest.

## ■ ACKNOWLEDGMENTS

This work was financially supported by the National Science and Technology Council (NSTC) in Taiwan (MOST 111-2221-E-011-011, NSTC 112-2221-E-011-016-MY3, and NSTC 112-2218-E-011-011), the Ministry of Education of Taiwan (Sustainable Electrochemical Energy Development (SEED) Center project), National Taiwan University of Science and Technology-Tokushima University Joint Research Program (TU-NTUST-2023-05), and industry-academia cooperation project (NTUST-Might Electronic-No. 10959). Research facilities of Hard-XAS was provided by the beamline of BL17C, National Synchrotron Radiation Research Center (NSRRC) in Taiwan. Thanks to Ms C.-Y. Chien of Ministry of Science and Technology (National Taiwan University) for the assistance in TEM experiments.

## ■ REFERENCES

- (1) Kim, J.; Campbell, A. S.; de Ávila, B. E.-F.; Wang, J. Wearable biosensors for healthcare monitoring. *Nat. Biotechnol.* **2019**, *37* (4), 389–406.
- (2) Sharma, A.; Badea, M.; Tiwari, S.; Marty, J. L. Wearable biosensors: an alternative and practical approach in healthcare and disease monitoring. *Molecules* **2021**, *26* (3), 748.
- (3) Seshadri, D. R.; Li, R. T.; Voos, J. E.; Rowbottom, J. R.; Alfes, C. M.; Zorman, C. A.; Drummond, C. K. Wearable sensors for monitoring the physiological and biochemical profile of the athlete. *NPJ. Digital Med.* **2019**, *2* (1), 72.
- (4) Heikenfeld, J. Non-invasive analyte access and sensing through eccrine sweat: Challenges and outlook circa 2016. *Electroanalysis* **2016**, *28* (6), 1242–1249.
- (5) Wang, Y.-X.; Rinawati, M.; Zhan, J.-D.; Lin, K.-Y.; Huang, C.-J.; Chen, K.-J.; Mizuguchi, H.; Jiang, J.-C.; Hwang, B.-J.; Yeh, M.-H. Boron-Doped Graphene Quantum Dots Anchored to Carbon Nanotubes as Noble Metal-Free Electrocatalysts of Uric Acid for a Wearable Sweat Sensor. *ACS Appl. Nano Mater.* **2022**, *5* (8), 11100–11110.
- (6) Kanokpaka, P.; Chang, L.-Y.; Wang, B.-C.; Huang, T.-H.; Shih, M.-J.; Hung, W.-S.; Lai, J.-Y.; Ho, K.-C.; Yeh, M.-H. Self-powered molecular imprinted polymers-based triboelectric sensor for non-invasive monitoring lactate levels in human sweat. *Nano Energy* **2022**, *100*, 107464.
- (7) Fall, B.; Sall, D. D.; Hémadi, M.; Diaw, A. K. D.; Fall, M.; Randriamahazaka, H.; Thomas, S. Highly efficient non-enzymatic electrochemical glucose sensor based on carbon nanotubes functionalized by molybdenum disulfide and decorated with nickel nanoparticles (GCE/CNT/MoS<sub>2</sub>/NiNPs). *Sens. Actuators Rep.* **2023**, *5*, 100136.
- (8) De la Paz, E.; Saha, T.; Del Caño, R.; Seker, S.; Kshirsagar, N.; Wang, J. Non-invasive monitoring of interstitial fluid lactate through an epidermal iontophoretic device. *Talanta* **2023**, *254*, 124122.
- (9) Bakker, J.; Gris, P.; Coffernils, M.; Kahn, R. J.; Vincent, J.-L. Serial blood lactate levels can predict the development of multiple organ failure following septic shock. *Am. J. Surg.* **1996**, *171* (2), 221–226.
- (10) Mizock, B. A.; Falk, J. L. Lactic acidosis in critical illness. *Crit. Care Med.* **1992**, *20* (1), 80–93.
- (11) Pereira, S. A.; Mota, F. A.; Çay, I.; Passos, M. L.; Araujo, A. R.; Saraiva, M. L. M. Automatic fluorometric lactate determination in human plasma samples. *New J. Chem.* **2020**, *44* (2), 543–548.
- (12) Rattu, G.; Krishna, P. M. Enzyme-free colorimetric nanosensor for the rapid detection of lactic acid in food quality analysis. *J. Agric. Food Res.* **2022**, *7*, 100268.
- (13) Nien, Y.-H.; Kang, Z.-X.; Su, T.-Y.; Ho, C.-S.; Chou, J.-C.; Lai, C.-H.; Kuo, P.-Y.; Lai, T.-Y.; Dong, Z.-X.; Chen, Y.-Y.; et al.

Investigation of Flexible Arrayed Lactate Biosensor Based on Copper Doped Zinc Oxide Films Modified by Iron–Platinum Nanoparticles. *Polymers* **2021**, *13* (13), 2062.

(14) Zhang, H.-Y.; Zhang, P.-P.; Tan, X.-X.; Wang, Z.-Z.; Lian, K.-Q.; Xu, X.-D.; Kang, W.-J. Derivatization method for the quantification of lactic acid in cell culture media via gas chromatography and applications in the study of cell glycometabolism. *J. Chromatogr. B* **2018**, *1090*, 1–6.

(15) Vaňkátová, P.; Kubičková, A.; Cigl, M.; Kalíková, K. Ultra-performance chromatographic methods for enantioseparation of liquid crystals based on lactic acid. *J. Supercrit. Fluids* **2019**, *146*, 217–225.

(16) Rathee, K.; Dhull, V.; Dhull, R.; Singh, S. Biosensors based on electrochemical lactate detection: A comprehensive review. *Biochem. Biophys. Rep.* **2016**, *5*, 35–54.

(17) Naresh, V.; Lee, N. A review on biosensors and recent development of nanostructured materials-enabled biosensors. *Sensors* **2021**, *21* (4), 1109.

(18) Prodromidis, M. I.; Karayannis, M. I. Enzyme based amperometric biosensors for food analysis. *Electroanalysis* **2002**, *14* (4), 241–261.

(19) Ahmed, J.; Rashed, M. A.; Faisal, M.; Harraz, F. A.; Jalalah, M.; Alsareii, S. Novel SWCNTs-mesoporous silicon nanocomposite as efficient non-enzymatic glucose biosensor. *Appl. Surf. Sci.* **2021**, *552*, 149477.

(20) Wang, H.; Li, Y.; Deng, D.; Li, M.; Zhang, C.; Luo, L. NiO-Coated CuCo<sub>2</sub>O<sub>4</sub> Nanoneedle Arrays on Carbon Cloth for Non-enzymatic Glucose Sensing. *ACS Appl. Nano Mater.* **2021**, *4* (9), 9821–9830.

(21) Li, Y.; Deng, D.; Wang, H.; Huan, K.; Yan, X.; Luo, L. Controlled synthesis of Cu-Sn alloy nanosheet arrays on carbon fiber paper for self-supported nonenzymatic glucose sensing. *Anal. Chim. Acta* **2022**, *1190*, 339249.

(22) Ye, J.; Deng, D.; Wang, Y.; Luo, L.; Qian, K.; Cao, S.; Feng, X. Well-aligned Cu@C nanocubes for highly efficient nonenzymatic glucose detection in human serum. *Sens. Actuators, B* **2020**, *305*, 127473.

(23) Huan, K.; Li, Y.; Deng, D.; Wang, H.; Wang, D.; Li, M.; Luo, L. Composite-controlled electrospinning of CuSn bimetallic nanoparticles/carbon nanofibers for electrochemical glucose sensor. *Appl. Surf. Sci.* **2022**, *573*, 151528.

(24) Long, X.; Wang, Z.; Xiao, S.; An, Y.; Yang, S. Transition metal based layered double hydroxides tailored for energy conversion and storage. *Mater. Today* **2016**, *19* (4), 213–226.

(25) Chala, S. A.; Tsai, M.-C.; Su, W.-N.; Ibrahim, K. B.; Duma, A. D.; Yeh, M.-H.; Wen, C.-Y.; Yu, C.-H.; Chan, T.-S.; Dai, H.; et al. Site activity and population engineering of NiRu-layered double hydroxide nanosheets decorated with silver nanoparticles for oxygen evolution and reduction reactions. *ACS Catal.* **2018**, *9* (1), 117–129.

(26) Rinawati, M.; Wang, Y.-X.; Chen, K.-Y.; Yeh, M.-H. Designing a spontaneously deriving NiFe-LDH from bimetallic MOF-74 as an electrocatalyst for oxygen evolution reaction in alkaline solution. *Chem. Eng. J.* **2021**, *423*, 130204.

(27) Wang, Y.-X.; Tsao, P.-K.; Rinawati, M.; Chen, K.-J.; Chen, K.-Y.; Chang, C. Y.; Yeh, M.-H. Designing ZIF-67 derived NiCo layered double hydroxides with 3D hierarchical structure for Enzyme-free electrochemical lactate monitoring in human sweat. *Chem. Eng. J.* **2022**, *427*, 131687.

(28) Wu, Y.-T.; Tsao, P.-K.; Chen, K.-J.; Lin, Y.-C.; Aulia, S.; Chang, L.-Y.; Ho, K.-C.; Chang, C. Y.; Mizuguchi, H.; Yeh, M.-H. Designing bimetallic Ni-based layered double hydroxides for enzyme-free electrochemical lactate biosensors. *Sens. Actuators, B* **2021**, *346*, 130505.

(29) Anantharaj, S.; Karthick, K.; Kundu, S. Evolution of layered double hydroxides (LDH) as high performance water oxidation electrocatalysts: A review with insights on structure, activity and mechanism. *Mater. Today Energy* **2017**, *6*, 1–26.

(30) Jian, S.-L.; Hsiao, L.-Y.; Yeh, M.-H.; Ho, K.-C. Designing a carbon nanotubes-interconnected ZIF-derived cobalt sulfide hybrid

nanocage for supercapacitors. *J. Mater. Chem. A* **2019**, *7* (4), 1479–1490.

(31) Jian, S.-L.; Huang, Y.-J.; Yeh, M.-H.; Ho, K.-C. A zeolitic imidazolate framework-derived ZnSe/N-doped carbon cube hybrid electrocatalyst as the counter electrode for dye-sensitized solar cells. *J. Mater. Chem. A* **2018**, *6* (12), 5107–5118.

(32) Liu, J.; Zhu, D.; Guo, C.; Vasileff, A.; Qiao, S. Z. Design strategies toward advanced MOF-derived electrocatalysts for energy-conversion reactions. *Adv. Energy Mater.* **2017**, *7* (23), 1700518.

(33) Gonçalves, J. M.; Martins, P. R.; Rocha, D. P.; Matias, T. A.; Juliao, M. S.; Munoz, R. A.; Angnes, L. Recent trends and perspectives in electrochemical sensors based on MOF-derived materials. *J. Mater. Chem. C* **2021**, *9* (28), 8718–8745.

(34) Power, A. C.; Gorey, B.; Chandra, S.; Chapman, J. Carbon nanomaterials and their application to electrochemical sensors: a review. *Nanotechnol. Rev.* **2018**, *7* (1), 19–41.

(35) Yeh, M.-H.; Li, Y.-S.; Chen, G.-L.; Lin, L.-Y.; Li, T.-J.; Chuang, H.-M.; Hsieh, C.-Y.; Lo, S.-C.; Chiang, W.-H.; Ho, K.-C. Facile synthesis of boron-doped graphene nanosheets with hierarchical microstructure at atmosphere pressure for metal-free electrochemical detection of hydrogen peroxide. *Electrochim. Acta* **2015**, *172*, 52–60.

(36) Wang, Y.-X.; Rinawati, M.; Huang, W.-H.; Cheng, Y.-S.; Lin, P.-H.; Chen, K.-J.; Chang, L.-Y.; Ho, K.-C.; Su, W.-N.; Yeh, M.-H. Surface-engineered N-doped carbon nanotubes with B-doped graphene quantum dots: Strategies to develop highly-efficient noble metal-free electrocatalyst for online-monitoring dissolved oxygen biosensor. *Carbon* **2022**, *186*, 406–415.

(37) Lu, L.; Zhou, L.; Chen, J.; Yan, F.; Liu, J.; Dong, X.; Xi, F.; Chen, P. Nanochannel-Confined Graphene Quantum Dots for Ultrasensitive Electrochemical Analysis of Complex Samples. *ACS Nano* **2018**, *12* (12), 12673–12681.

(38) Su, X.; Chan, C.; Shi, J.; Tsang, M.-K.; Pan, Y.; Cheng, C.; Gerile, O.; Yang, M. A graphene quantum dot@Fe<sub>3</sub>O<sub>4</sub>@SiO<sub>2</sub> based nanoprobe for drug delivery sensing and dual-modal fluorescence and MRI imaging in cancer cells. *Biosens. Bioelectron.* **2017**, *92*, 489–495.

(39) Huang, Q.; Lin, X.; Tong, L.; Tong, Q.-X. Graphene Quantum Dots/Multiwalled Carbon Nanotubes Composite-Based Electrochemical Sensor for Detecting Dopamine Release from Living Cells. *ACS Sustainable Chem. Eng.* **2020**, *8* (3), 1644–1650.

(40) Lin, Y.-C.; Rinawati, M.; Chang, L.-Y.; Wang, Y.-X.; Wu, Y.-T.; Yen, Y.-H.; Chen, K.-J.; Ho, K.-C.; Yeh, M.-H. A non-invasive wearable sweat biosensor with a flexible N-GQDs/PANI nanocomposite layer for glucose monitoring. *Sens. Actuators, B* **2023**, *383*, 133617.

(41) Tarigan, A. M.; Aulia, S.; Rinawati, M.; Chang, L.-Y.; Cheng, Y.-S.; Chang, C.-C.; Huang, W.-H.; Chen, J.-L.; Setyawan, H.; Yeh, M.-H. Tandem surface engineering of graphene quantum dot-assisted fluorinated NiFe Prussian blue analogue for electrocatalytic oxygen evolution reaction. *Chem. Eng. J.* **2023**, *476*, 146754.

(42) Ahirwar, S.; Mallick, S.; Bahadur, D. Electrochemical Method To Prepare Graphene Quantum Dots and Graphene Oxide Quantum Dots. *ACS Omega* **2017**, *2* (11), 8343–8353.

(43) Li, K.; Liu, W.; Ni, Y.; Li, D.; Lin, D.; Su, Z.; Wei, G. Technical synthesis and biomedical applications of graphene quantum dots. *J. Mater. Chem. B* **2017**, *5* (25), 4811–4826.

(44) Li, Y.; Zhao, Y.; Cheng, H.; Hu, Y.; Shi, G.; Dai, L.; Qu, L. Nitrogen-doped graphene quantum dots with oxygen-rich functional groups. *J. Am. Chem. Soc.* **2012**, *134* (1), 15–18.

(45) Claramunt, S.; Varea, A.; Lopez-Diaz, D.; Velázquez, M. M.; Cornet, A.; Cirera, A. The importance of interbands on the interpretation of the Raman spectrum of graphene oxide. *J. Phys. Chem. C* **2015**, *119* (18), 10123–10129.

(46) Zurrer, T.; Wong, K.; Horlyck, J.; Lovell, E. C.; Wright, J.; Bedford, N. M.; Han, Z.; Liang, K.; Scott, J.; Amal, R. Mixed-metal MOF-74 templated catalysts for efficient carbon dioxide capture and methanation. *Adv. Funct. Mater.* **2021**, *31* (9), 2007624.

(47) Sun, H.; Chen, L.; Lian, Y.; Yang, W.; Lin, L.; Chen, Y.; Xu, J.; Wang, D.; Yang, X.; Rümmerli, M. H.; et al. Topotactically transformed polygonal mesopores on ternary layered double



hydroxides exposing under-coordinated metal centers for accelerated water dissociation. *Adv. Mater.* **2020**, 32 (52), 2006784.

(48) Jiang, H.; He, Q.; Li, X.; Su, X.; Zhang, Y.; Chen, S.; Zhang, S.; Zhang, G.; Jiang, J.; Luo, Y.; et al. Tracking structural self-reconstruction and identifying true active sites toward cobalt oxychloride precatalyst of oxygen evolution reaction. *Adv. Mater.* **2019**, 31 (8), 1805127.

(49) Huang, L.; Chen, D.; Luo, G.; Lu, Y. R.; Chen, C.; Zou, Y.; Dong, C. L.; Li, Y.; Wang, S. Zirconium-Regulation-Induced Bifunctionality in 3D Cobalt–Iron Oxide Nanosheets for Overall Water Splitting. *Adv. Mater.* **2019**, 31 (28), 1901439.

(50) He, Y.; Liu, X.; Chen, G.; Pan, J.; Yan, A.; Li, A.; Lu, X.; Tang, D.; Zhang, N.; Qiu, T.; et al. Synthesis of Co (II)-Fe (III) hydroxide nanocones with mixed octahedral/tetrahedral coordination toward efficient electrocatalysis. *Chem. Mater* **2020**, 32 (10), 4232–4240.

(51) Bo, X.; Hocking, R. K.; Zhou, S.; Li, Y.; Chen, X.; Zhuang, J.; Du, Y.; Zhao, C. Capturing the active sites of multimetallic (oxy) hydroxides for the oxygen evolution reaction. *Energy Environ. Sci.* **2020**, 13 (11), 4225–4237.

(52) Yang, J.; Lei, C.; Liu, X.; Zhang, J.; Sun, Y.; Zhang, C.; Ye, M.; Zhang, K. Versatile Performance of a Cationic Surfactant Derived from Carbon Quantum Dots. *Acta Phys. -Chim. Sin.* **2021**, 38, 2111030.

(53) Brezko, J.; Grzeskiewicz, B.; Gradzka, E.; Bobrowska, D. M.; Basa, A.; Goclon, J.; Winkler, K. Synthesis of polyaniline nanotubes decorated with graphene quantum dots: Structural & electrochemical studies. *Electrochim. Acta* **2021**, 388, 138614.

(54) Shah, S. S. A.; El Jery, A.; Najam, T.; Nazir, M. A.; Wei, L.; Hussain, E.; Hussain, S.; Rebah, F. B.; Javed, M. S. Surface engineering of MOF-derived FeCo/NC core-shell nanostructures to enhance alkaline water-splitting. *Int. J. Hydrogen Energy* **2022**, 47 (8), 5036–5043.

(55) Wang, S.; Shang, J.; Wang, Q.; Zhang, W.; Wu, X.; Chen, J.; Zhang, W.; Qiu, S.; Wang, Y.; Wang, X. Enhanced electrochemical performance by strongly anchoring highly crystalline polyaniline on multiwalled carbon nanotubes. *ACS Appl. Mater. Interfaces* **2017**, 9 (50), 43939–43949.